ORIGINAL ARTICLE

Indentation-Derived Creep Response of Age-Hardened AlSi10Mg Fabricated Through Powder Bed Fusion Process

C. Vanitha[1] · **Vadapally Rama Rao**[1] · **C. Sashank**[1] ·
Deepak K. Pattanayak[2]

Abstract This work mainly focuses on investigating the microstructural and indentation creep behaviour of heat-treated AlSi10Mg alloy processed via the laser-assisted powder bed fusion (PBF) route. The as-built AlSi10Mg samples were initially solutionized at 520 °C for 2 h. Then, the solutionized samples were aged at 180 °C for 2 h. Indentation creep tests were conducted on the aged sample at three different loads 55, 92 and 129 MPa at 100 °C for 2 h. The steady-state creep rate was calculated from the slope of time vs indentation depth graph. In order to supplement the indentation creep results, detailed microstructural analysis has been carried out through optical and scanning electron microscopy. XRD study was carried out for phase analysis. AlSi10Mg in the as-built condition revealed the eutectic mixture at the melt pool boundaries and ultrafine Al cells in the interior. XRD pattern confirmed the presence of Mg_2Si in the age-hardened condition. Several defects were seen in the age-hardened condition. As-built alloy showed the highest hardness, whereas age hardening reduced the hardness due to the spheroidization of Si particles. The primary creep region showed an increase in indentation depth increased with respect to time. The depth of indentation remained constant in the secondary creep region. Age-hardened samples subjected to 92 MPa stress showed better creep resistance compared to 55 and 129 MPa. As-built condition showed the highest hardness due to the extremely fine microstructure.

✉ C. Vanitha
vanitha@nitw.ac.in

✉ Deepak K. Pattanayak

1   Department of Metallurgical and Materials Engineering, NIT Warangal, Hanamkonda 506004, India

2   CSIR-Central Electrochemical Research Institute, Karaikudi 630006, Tamil Nadu, India

1 Introduction

One of the most popular laser powder bed fusion (LPBF) based additive manufacturing techniques is Selective Laser Melting (SLM). Manufacturing of aluminium and its alloys through the SLM route has always been a tough challenge due to the rapid oxide layer formation. As a result, strong laser strengths are used to break these oxide layers [1]. AlSi10Mg alloy is one of the widely preferred alloys for making components such as pistons, heat exchangers, etc. owing to their high strength-to-weight ratio, corrosion resistance and low thermal expansion coefficient [2, 3].

At high temperatures, the phenomenon of creep plays an important role in predicting their lifetime before any failure. In AlSi10Mg alloy, eutectic silicon particles are responsible for providing good creep strength [4]. Hence, a thorough investigation of the creep performance of AlSi10Mg alloy as a function of corresponding microstructural changes is of high interest. Among various existing creep testing methods, the indentation creep test has several advantages over other techniques which can very easily assess the creep behaviour of both single crystal and polycrystalline materials. One can easily calculate thermal activation parameters like stress exponent, activation energy, etc. thereby predicting the mechanism of creep damage [5–9].

Ferrar et al. studied the reproducibility of the properties of SLMed AlSi10Mg alloys [10]. Read et al. optimized the process parameter through statistical exploratory approaches and as a result reduction in pores size was achieved, and mechanical properties were also evaluated [11]. Vincent Hammond et al. studied the effect of process interruptions of

SLM-processed specimens and found that the samples produced in the interrupted processing showed lower mechanical properties [12]. Uzana et al. have investigated the mechanical properties of SLM-processed AlSi10Mg alloy and found that dislocation motions in aluminium grains control the permanent deformation during creep [13]. Tae Hyun Park et al. observed that the sample processed through direct aging heat treatment enhanced the fatigue properties through modifying the Si morphology [14]. Dongming Li et al. examined the influence of temperature and time on the microstructures. With an increase in heat treatment temperature and time, a transformation of unique Si-rich melt pool boundaries into coarse particles took place [15]. Rama Rao et al. investigated the indentation creep behaviour at 100 °C on the as-built and solution heat-treated SLMed AlSi10Mg alloy. It was observed that the as-built alloy provided better creep resistance than the SHT condition [16]. Shakil et al. studied the indentation derived creep response of cast and LPBF processed AlSi10Mg and observed that the as-built one showed the least creep deformation as compared to the cast samples [17].

Heat exchanger and automobile components made up of AlSi10Mg alloys, undergoes ageing during service condition. An indentation test which is convenient, reliable to assess the deformation in a reasonable time scale compared to the conventional creep test has been used in the current study [16–19]. As the literature was limited to the hot indentation creep behaviour of SLM-built AlSi10Mg alloy [16], an effort was taken to study the same. Additionally, an attempt has been made to associate the changes in hot indentation creep behaviour of age-hardened AlSi10Mg with the alterations in silicon morphology when subjected to loads at 100 °C.

2 Experimental Methods

2.1 Material Fabrication and Heat Treatment

Cylindrical samples with 10 mm height and 15 mm diameter were SLM fabricated with a laser power of 370 watts and 0.03 mm thick powder bed, 0.19 mm hatch spacing and 1300 mm/s scan speed using pre-alloyed AlSi10Mg powder with spherical particles of two different sizes of 30 and 10 μm. The elements present in the pre-alloyed powder is described in Table 1.

The SLMed AlSi10Mg cylindrical test specimens were exposed to solution heat treatment (SHT) for 2 h at 520 °C and then age hardened at 180 °C for 2 h.

2.2 Density

Theoretical and relative density has been calculated using the density measured by Archimedes principle using (Sartorious-BSA224S-CW) weighing machine.

2.3 Metallography

An optical and scanning electron microscope was used to view the resulting microstructure of the samples polished according to the standard procedure followed by etching using Keller's reagent. EDS analysis was also carried out to estimate the elemental composition.

2.4 XRD Analysis

Samples were scanned using Panalytical (Model-X'pert) X-ray diffractometer. Crystallite size and lattice strain calculations were also performed using Scherrer expression. By plotting $\beta_T \cos\theta$ against $4\sin\theta$, also called as Williamson-Hall plot, one can get a straight line with slope ε and the calculated slope provides the lattice strain. β_T is the total broadening due to the broadening due to lattice strain and broadening due to crystallite size [20].

The dislocation density (δ) was calculated from microstrain (ε) and crystallite size (D) values as obtained from XRD studies using the following expression below:

$$\delta = \frac{2\sqrt{3} * (\varepsilon^2)^{\frac{1}{2}}}{D * b} \tag{1}$$

where, b—the magnitude of the Burgers vector $= a_0/\sqrt{2}$ (for an FCC alloy) a_0—the lattice constant [21].

2.5 Hot Indentation Creep Test

The indentation creep test carried out at 100 °C at loads of 55, 92 and 129 MPa. Load was applied for 4 h. An LVDT sensor recorded the changes in depth of indentation with respect to time. The slope of depth of indentation versus time provides the steady state creep rate.

2.6 Hardness Measurement

Vicker's micro-hardness tester of model (HMV-G20ST) was used. Vickers micro-hardness values were determined. A 100-g load was applied for 10 s.

Table 1 Elemental composition of pre-alloyed powder supplied by EOS Gmbh

Elements	Al	Si	Mg	Fe	Mn	Ti	Zn	Ni	Pb	Sn	Cu
Wt.%	Bal	8–11	0.25–0.45	0.55	0.45	0.15	0.1	0.05	0.05	0.05	0.05

Yield strength was calculated for as-built, solutionized and aged samples based on the relationship suggested by Cahoon et al. [22], which is given by:

$$\sigma_y = \left(\frac{VH}{3}\right) * (0.1)^n$$

where σy—Yield strength (MPa)

VH—Vickers hardness (MPa) and n—strain hardening coefficient, whose value is considered to be 0.1 for SLM-built and heat-treated SLM processed AlSi10Mg specimens [23].

3 Results and Discussion

3.1 Density

The relative density of the as-built samples was $98.6 \pm 0.9\%$. By contrast, after SHT heat treatment and age hardening, the relative densities were 99.43 ± 0.2 and $99.1 \pm 0.1\%$, respectively. The as-built conditions show less density due to the presence of pores [24]. However, in the case of age hardening, the density got reduced because of the small pores formed due to the difference in thermal expansion coefficient between the aluminium cells and Si particles.

3.2 Microstructural Features

Figure 1a and b shows the optical microstructure of the longitudinal and transverse plane of the as-built AlSi10Mg, respectively. The longitudinal plane revealed the scan track and pores of different shapes. The melt boundary consists of the eutectic mixture and the core revealed very fine grains (see Fig. 1a). The transverse plane revealed a fish scale morphology that arose due to the repeated melting and cooling (see Fig. 1b). As shown in Fig. 2a, the SHT image had only a few melt pool boundaries, i.e. after SHT, the melt pools present in the microstructure were found to be dispersed as compared to the as-built condition. Fig. 2b shows the OM image in the age hardened condition and one can observe from this image that the melt pool boundaries vanished and the melt pool eutectic silicon disintegrated into the more distinct Si particles in the aluminium matrix.

These melt pools are basically the inhomogeneity present in the microstructure which was formed due to high localized melting and rapid solidification [25]. Figure 3a shows the SEM image in the as-built condition. The microstructure shows two distinct regions, i.e. one region has coarse cells,
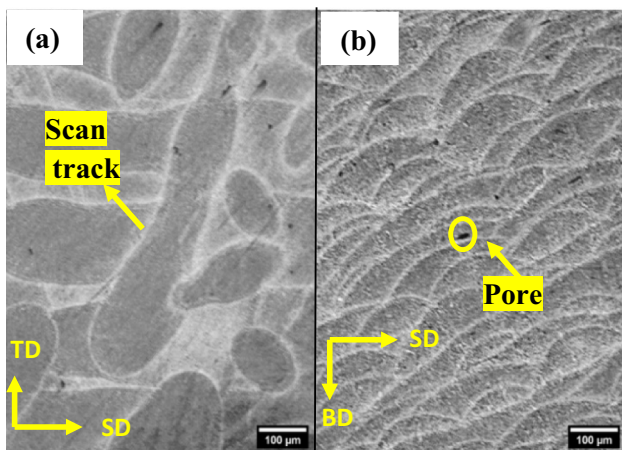

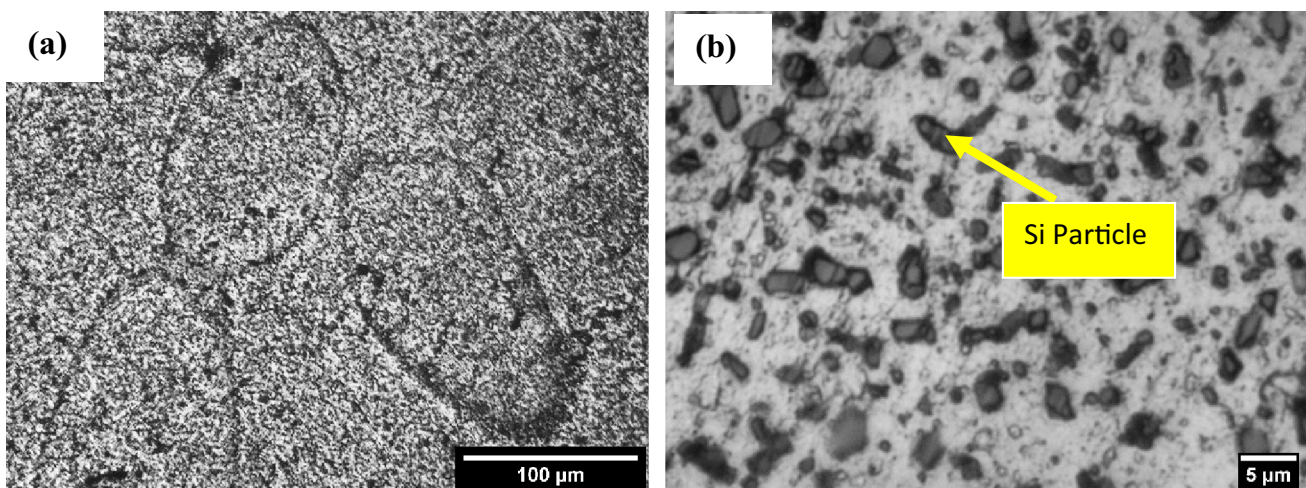**Fig. 1** OM image of as-built condition. (**a**) Longitudinal, (**b**) transverse plane

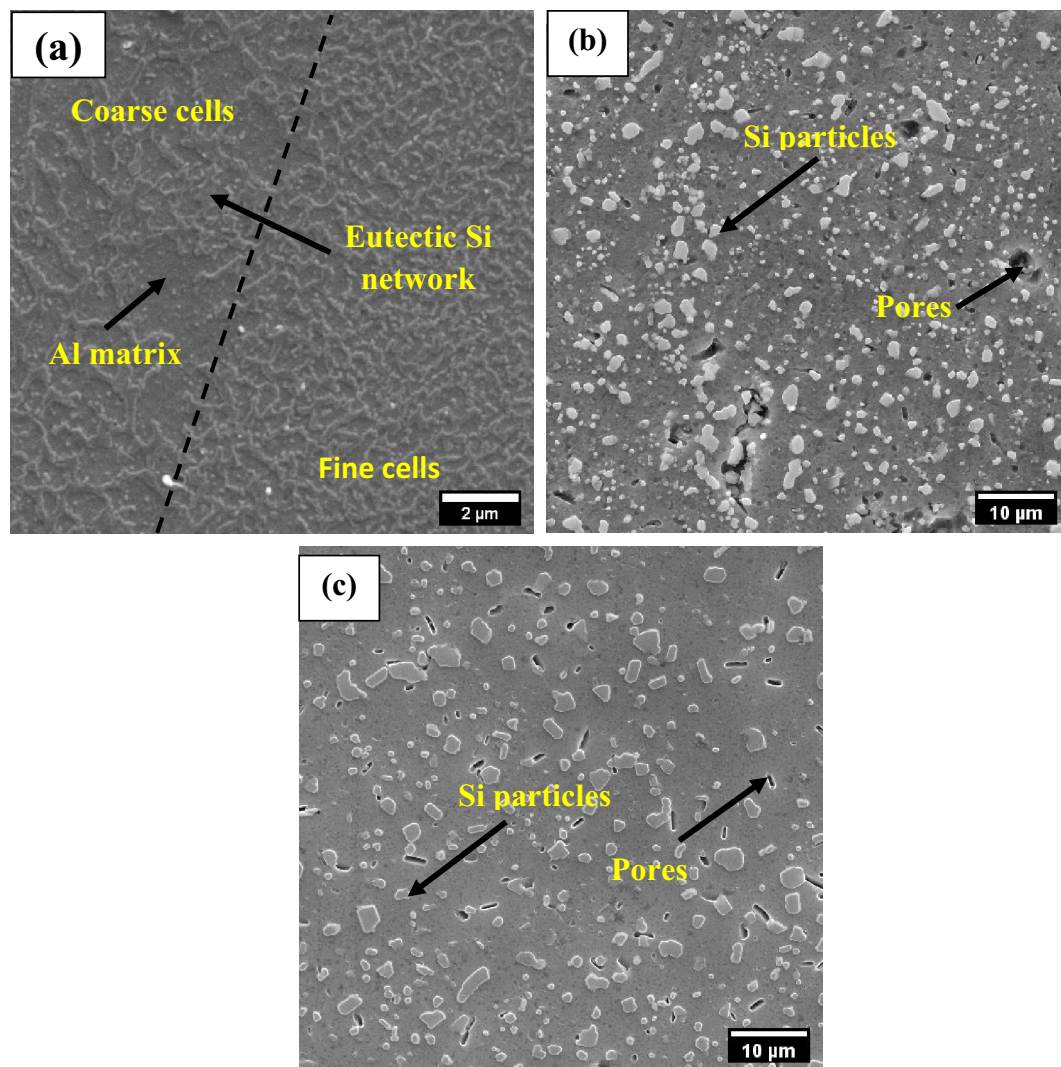**Fig. 2** OM image in (**a**) SHT-520 °C/2 h/WQ (**b**) Aged/180 °C/2 h

Fig. 3 SEM image of AlSi10Mg alloy (**a**) As-built condition, (**b**) SHT (**c**) age hardened condition

whereas the other region has very fine cells. Coarse cells are formed at the melt pool boundary region. Fine cells are formed in the region interior to the melt pool. Very fine cells are formed due to the cooling rates of 10^6 K/s during the SLM process. Fine cells of 0.49 μm size were surrounded by a continuous fibrous silicon network 0.18 μm wide.

EDS studies carried out on different regions of melt pools confirmed that the continuous fibrous network contains eutectic Si, whereas the cells are identified as aluminium. Figure 3b shows SEM image of solution heat-treated AlSi10Mg alloy in which continuous fibrous eutectic Si network in the as-built microstructure transformed into near spherical-shaped Si particles and was seen everywhere. This change in the morphology of Si from fibrous form to particulate form is termed as spheroidization, which might be attributed to the phenomenon of diffusion of Si at high temperatures during SHT. The average particle size of the coarse

particles and fine Si particles formed after solutionizing was found to be 2.2 ± 0.7 μm and 0.78 ± 0.1 μm respectively. In addition, pores were also noticed in the microstructure. Figure 3c shows SEM image of AlSi10Mg alloy after ageing. It can be noted that the Si particles formed during solutionizing got much more uniformly distributed and widely spaced after ageing. The aged microstructure shows three distinct morphologies of Si particles: fine spherical particles, coarse spherical particles and elongated particles. It is also evident that after ageing treatment, Si particles became coarser when compared to the solutionized condition which might be attributed to the phenomenon of grain coarsening, coalescence, and Ostwald ripening [26–29]. The average particle size of the coarse and fine Si particles formed after ageing was found to be 2.6 ± 0.2 μm and 0.866 ± 0.1 μm, respectively, which is comparatively larger compared to the SHT condition. Additionally, it could be observed that the number

of pores present in the aged AlSi10Mg microstructure was much higher than those in the solutionized microstructure.

As shown in Fig. 4a, the microstructure of the non-indenter contact region or undeformed region shows three different morphologies of Si particles: fine, coarse and elongated Si particles. The average particle size of the coarse, fine and elongated Si particles in the non-indenter exposed or undeformed region after the hot indentation creep test was measured to be about 2.9 ± 0.4, 1.1 ± 0.2 and 2.5 ± 0.1 to 4 ± 0.4 μm, respectively. Irrespective of the applied stress, the average particle size obtained in the non-impressed or undeformed region was higher than in the indented or deformed region. Thus, it can be inferred that coarsening of Si particles has occurred in this undeformed region during the 4 h dwell time at the test temperature of 100 °C. It can also be observed that the pore size has also considerably increased in the undeformed region after the hot indentation creep test.

Figure 4(b)-(d) shows the SEM images of the deformed region which was in contact with the indenter of aged AlSi10Mg samples subjected to hot indentation creep test at 100 °C for 4 h at 55, 92 and 129 MPa, respectively. Several deformation bands were clearly visible in the microstructures. Both applied stress, test temperature and dwell time significantly influence the formation of deformation bands and Si morphology on the microstructure of the deformed region. The severity of deformation bands formed increases with an increase in the load applied, since the higher the applied load, higher the plastic flow.

After the hot indentation test, there was a change in the morphology of the Si particles into rod-shaped structure irrespective of applied stress. This can be mainly attributed to the phenomenon of segregation of small particles to form larger ones at the test temperature and time. Initially, diffusion of the discrete silicon particles at the melt pool boundary takes a rod shape during the indentation dwell period. In addition to that there is a reduction in the size and volume fraction of the Si particles in the matrix, the applied load is transferred from the aluminium matrix to the silicon rod, and subsequently, there is a crack initiated on the surface of the silicon rod.

As the aluminium matrix is ductile and the silicon rod is brittle the matrix deforms and the silicon rod breaks on application of 55 MPs load. The volume fraction of Si rods

Fig. 4 SEM images of age hardened and hot indentation tested samples (**a**) 0 MPa/non-indenter contact region (**b**) 55, (**c**) 92 and (**d**) 129 MPa
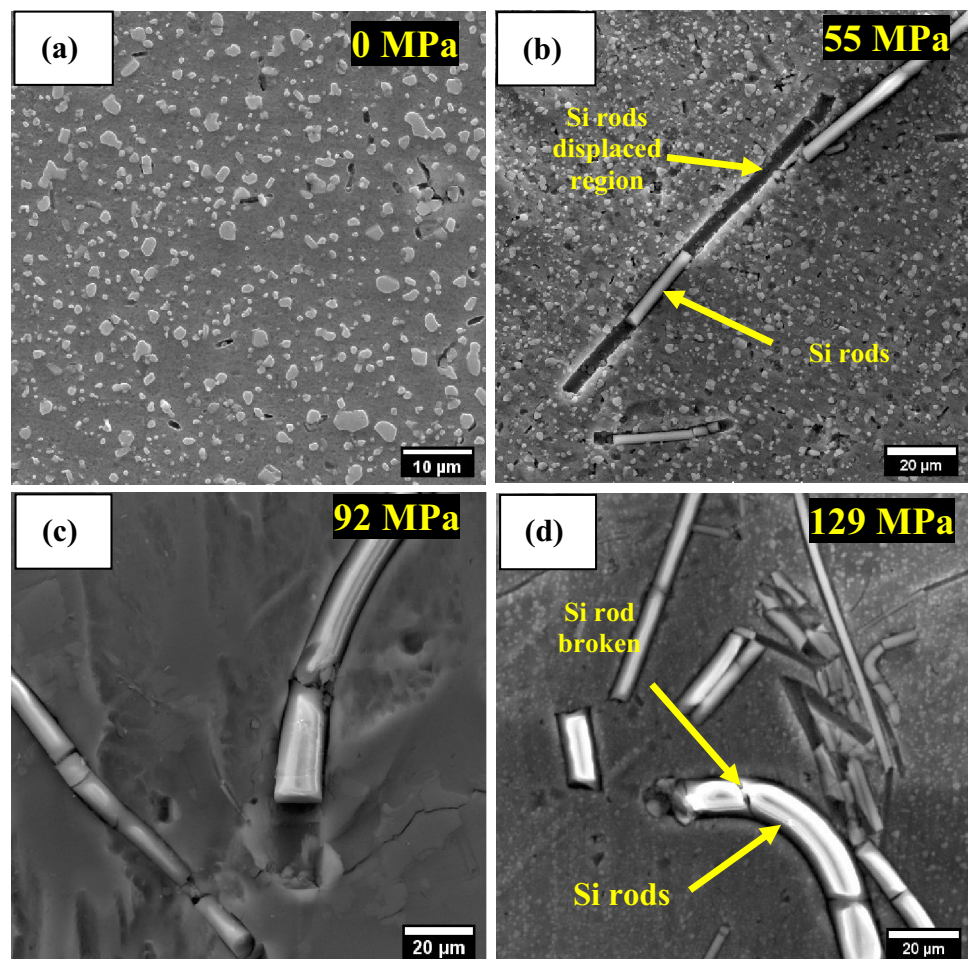
was found to be maximum for an applied stress of 129 MPa when compared to the other two loads applied (see Fig. 4d). It was also observed that the Si rod got displaced from its location irrespective of the load applied.

3.3 XRD Analysis

The as-built sample has the maximum lattice strain of 0.63835×10^{-3}, whereas the heat-treated samples (both solutionized and age hardened) have comparatively lower values of lattice strain when compared to as-built conditions. This shows that upon heat treatment, stress relieving has taken place. It can also be observed that the sample after solutionizing at 520 °C for 2 h shows a lattice strain value of about 0.5653×10^{-3}, whereas those samples aged (at 100 and 180 °C) after the same solutionizing treatment have been found to have lower lattice strain values (0.49548×10^{-3}). This shows that ageing after solutionizing plays an eminent role in relieving the stresses in the strained lattice as shown in Table 2.

The dislocation density calculated from the XRD analysis is given in Table 2. It clearly indicates that the dislocation density was 5.761×10^{14} m^{-2} in the as-built condition. However, upon solutioning the dislocation density reduced by 17% and on ageing it reduced 31%. Because of the high cooling rate, the microstructure revealed the very fine aluminium cells surrounded by the silicon network. The Si network acts as an efficient dislocation obstacle and hence the dislocation movement is restricted.

However, during solutionizing, the silicon network turned into particles and during ageing the particles got coarsened. Coarse particles which are widely spaced always allow the dislocation to move freely and hence the dislocation density is low and possess lesser hardness as compared to the as-built samples.

3.4 Hot Indentation Creep Behaviour

Figure 5 gives the effect of load on the depth of indentation with respect to time of age-hardened samples hot indentation tested at 100 °C tested for 4 h. The creep curve was found to have two distinct regions: primary creep
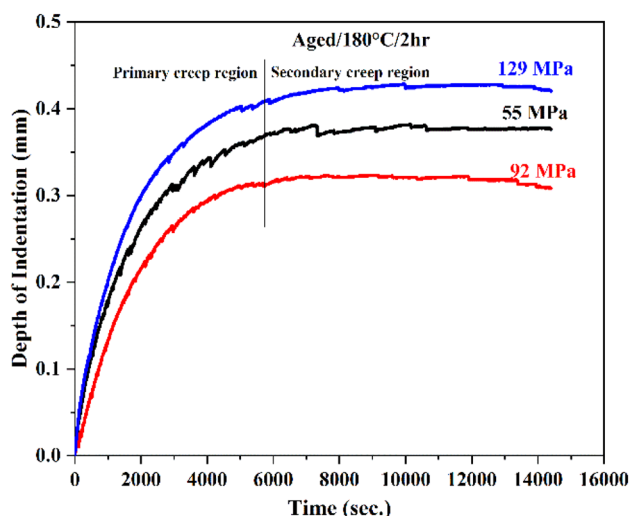

Fig. 5 Effect of load on the depth of indentation

region and secondary creep region. It can also be observed that irrespective of the load applied and temperature, the depth of indentation increased rapidly with an increase in time in the primary creep region, whereas in the secondary creep region, the depth of indentation was found to remain constant.

For a given test temperature of 100 °C, the depth of indentation was minimum, i.e. 0.3 mm when the load applied was 92 MPa, whereas a maximum depth of indentation of 0.42 mm was obtained when the load applied was 129 MPa. However, when the load applied was 55 MPa, the depth of indentation obtained was 0.37 mm. When the load increased from 92 to 129 MPa, the depth of indentation got increased by 13.5%. This irregular trend in the depth of indentation with respect to the load applied can be attributed to the irregular trend in the Si particle size observed with respect to load applied.

The indentation creep rate of the aged sample in the current study was 3.68×10^{-7}/s for an applied stress of 55 MPa. From Table 3, it is clearly evident that irrespective of the load applied, the aged condition offered better indentation creep resistance when compared to as-built and SHT conditions.

Table 2 Dislocation density for different heat treatment condition

Samples	Crystallite size D (nm)	Micro-strain ε (%)	Lattice constant a_o (nm)	Dislocation density δ ($* 10^{18}$ m^{-2})	Dislocation density δ ($* 10^{14}$ m^{-2})
As-built	134.09	0.638	0.405	0.0006	5.761
SHT-520 °C/2 h	143.38	0.5653	0.405	0.0005	4.772
SHT-520 °C/2 h + Aged/180 °C/2 h	149.56	0.4954	0.406	0.0004	3.994

Table 3 Comparison of steady-state creep rate values in the present study with the available literature

Applied stress (MPa)	Steady-state creep rate (/s)		
	Aged condition [Current study]	Built condition [16]	SHT condition [16]
55	3.68×10^{-7}	1.20×10^{-5}	4.00×10^{-5}
92	3.60×10^{-7}	2.10×10^{-5}	4.50×10^{-5}
129	3.73×10^{-7}	3.20×10^{-5}	5.00×10^{-5}

Table 4 Maximum depth of indentation

Stress (MPa)	Maximum depth of indentation, h (mm)		
	Aged condition [Current study]	Built condition [16]	SHT condition [16]
55	0.381	0.052	0.285
92	0.323	0.114	0.365
129	0.428	0.191	0.404

This hike in the creep rate of aged AlSi10Mg as compared with the as-built condition can be attributed to the presence of coarse Si particles formed during ageing and also due to the larger distance between the particles . As the Si network present in the continuous form also acts as an obstacle for the dislocation motion and hence the as-built AlSi10 alloy shows better creep resistance than the age-hardened alloy. In addition to the role of dislocation barrier of the Si network, the super saturated alloying elements also cause solid solution strengthening in the as-built sample. The solid solution strengthening is also weak in case of SHT and age-hardened conditions, due to the coarse nature of the Si particles.

Table 4 gives the comparison between measured depth of indentation of as built, SHT and age-hardened samples. It can be observed that, at a constant load of 55 MPa, the maximum indentation depth within the materials (h) is the highest in the aged sample and the smallest in the as-built sample (i.e., $h_{\text{as-built}} < h_{\text{SHT}} < h_{\text{aged}}$). The same trend follows for all other applied loads too. This maximum depth of indentation value obtained is directly related to the mechanical properties of the material being tested, especially the hardness and yield strength. The age-hardened

samples show less resistance to depth of indentation as compared with SHT is due to the coarsening of the Si particles and due to the weak solid solution strengthening.

3.5 Hardness—Yield Strength Co-relation

Table 5 shows the measured Vickers hardness values for as built, SHT and age-hardened samples. It can be noticed that the Vickers hardness (VH) value for as-built sample was 115 ± 3.2 HV, whereas the same for the solutionized and aged samples were found out to be 86 ± 0.2 and 84 ± 0.2 HV, respectively. Similarly, the yield strength value for as-built sample was 298 MPa, whereas the same for solutionized and aged samples were 224 and 219 MPa, respectively.

This highest hardness and yield strength values in as-built samples can be explained in terms of the SLM processing conditions. Since the as-built sample was subjected to a very high cooling rate of 10^6 K/s, higher cooling rate results a microstructure that consists of very fine cellular α aluminium. The fibrous eutectic Si particles surrounding the aluminium cells thereby promote grain boundary strengthening. A combination of solid solution strengthening and the resistance offered by the eutectic Si particles for the dislocation motion imparts high hardness and yield strength to it [17, 24, 30, 31].

Whereas heat-treated samples both solutionized and aged ones were found to have comparatively lower hardness values, i.e. they were softer than the as-built sample. Among all, the age-hardened sample was found to have the lowest hardness value [24]. This can be attributed to the formation of coarser Si particles due to coalescence at higher temperatures which further counters the strengthening effects in the SLM processed as-built samples, thereby causing a reduction in their hardness and yield strength values. The drop in the strength upon heat treatment is due to the softening effects mainly caused due to Si spheroidization, grain growth and the elimination of solid-solution strengthening [27, 31]. In the case of conventional alloy, the T6 heat treatment is carried out to enhance the strength. Contrary to previous findings, T6 heat-treated SLM-fabricated AlSi10Mg can lead to softening rather than hardening in cast alloys [32, 33]

Table 5 Vickers hardness and yield strength values for as-built, SHT and aged AlSi10Mg

Mechanical properties	Built condition	SHT condition	Aged condition
Vickers hardness, VH (MPa) [Experimental]	1128	846	827
Yield strength, σ_y (MPa) [Calculated]	298	224	219

4 Conclusions

Based on the analysis of the experimental results obtained, the following can be drawn:

- OM image of the as-built condition showed the melt pool boundaries or the scan track. SEM image revealed the eutectic mixture at the melt pool boundaries. The core of the melt pool boundaries consisted of ultrafine Al cells of about 0.6 μm surrounded by the Si continuous network with a boundary width of about 0.3 μm.

- Coarser Si particles were distantly observed in age-hardened samples.XRD pattern revealed the presence of Al, Si and Mg_2Si in the age-hardened condition

- At any applied load, the deformed region revealed the rod morphology. The undeformed region revealed the particle morphology.

- The depth of indentation increased significantly with an increase in the time in the primary creep region and remained constant in the secondary creep region. Age-hardened samples subjected to 92 MPa stress showed better creep resistance compared to 55 and 129 MPa.

- High creep rate of aged AlSi10Mg can be attributed to the presence of coarse Si particles, a large distance between the particles and a weak solid solution effect in age-hardened samples.

- The volume fraction of Si was more at a lower load. However, the volume fraction of rods displaced from their position was more at a higher load.

- The hardness value of the as-built condition, SHT and age-hardened samples were about 115, 86 and 84 HV, respectively. Age-hardening reduced the hardness due to the spheroidization and growth of Si particles

Declaration

Conflict of interest The authors declare that they have no known competing financial interests or personal relationships that could have appeared to influence the work reported in this paper.

References

1. Louvis Eleftherios, Fox Peter & Sutcliffe Christopher J. *Journal of Mater. Process. Tech.* 211 (2011) 275-284. https://doi.org/10.1016/j.jmatprotec.2010.09.019

2. Ayush Sinha, Biswajit Swain, Asit Behera, Priyabrata Mallick, Saswat Kumar Samal, Vishwanatha H M & Ajit Behera, *J. Manuf. Mater. Process.* **6**(1), (2022) 1-34. https://doi.org/10.3390/jmmp6010016.

3. Krystian Zyguła, Bartłomiej Nosek, Hubert Pasiowiec & Norbert Szysiak, *World Scientific News*, **104** (2018) 456-466, EISSN 2392–2192.

4. Gupta A K, Lloyd D J & Court S A, Precipitation hardening in Al–Mg–Si alloys with and without excess Si. *Mater. Sci. and Engg. A* **316** (2001) 11-17. https://doi.org/10.1016/S0921-5093(01)01247-3

5. Sai Deepak Kumar A, Fayaz Anwar Mohammad, Vara Prasad E, Bharath Sreevatsava P & Vanitha C, *Mater. Today: Proc.* **93** (2021) 1292-1302, https://doi.org/10.1016/j.matpr.2020.04.366

6. James Anthony LaManna Jr., Doctoral thesis on "A Study of the Relationship between Indentation Creep and Uniaxial Creep", University of Tennessee, Knoxville.(Knoxville, USA) 2006, 163 , https://trace.tennessee.edu/utk_graddiss/1973, accessed 14th January 2023

7. Yan Wuzhu, Wen Shifeng, Liu Jun & Yue Zhufeng, . *Mater. Sci. and Engg. A* **527**(2010) 1850-1855. https://doi.org/10.1016/j.msea.2009.11.035.

8. Bharath Sreevatsava P, and Vara Prasad E, Sai Deepak Kumar A, Mohammad Fayaz Anwar, Vadapally Rama Rao & Vanitha C, *Metall. Mater. Eng.* **27**(4), (2021) 531-539. https://doi.org/10.30544/745.

9. Yu H Y, Imam M A, & Rath B B, , An impression test method for characterisation of the flow behaviour of superplastic material, *Mater. Sci. and Engg.* **79**(2), (1986) 125-132. https://doi.org/10.1016/0025-5416(86)90395-2.

10. Ferrar B, Mullen L, Jones E, Stamp R & Sutcliffe C J, *J. of Mater. Process. Tech.* **212** (2012) 355-364. https://doi.org/10.1016/j.jmatprotec.2011.09.020

11. Read N, Wang W, Essa K & Attallah MM, *Mater. & Des.* **65**, (2015) 417–424. https://doi.org/10.1016/j.matdes.2014.09.044.

12. Hammond Vincent, Schuch Michael & Bleckmann Matthias, The influence of a process interruption on tensile properties of AlSi10Mg samples produced by selective laser melting. *Rapid Proto. J.* **25**(8), (2019) 1442–1452. https://doi.org/10.1108/RPJ-04-2018-0105

13. Naor Elad Uzana, Roni Shnecka, Ori Yeheskelb & Nachum Frage, *Addit. Manuf.* **24** (2018) 257-263. https://doi.org/10.1016/j.addma.2018.09.033

14. Tae-Hyun Park, Min-Seok Baek, Holden Hyer, Yongho Sohn & Kee-Ahn Lee, *Mater. Charac.* **176** (2021) 111113,1-10. https://doi.org/10.1016/j.matchar.2021.111113.

15. Dongming Li, Ruixian Qin, Jianxin Xu, Bingzhi Chen & Xu Niu, *Mater. Charac.* **187** (2022) 111882,1-13. https://doi.org/10.1016/j.matchar.2022.111882.

16. Vadapally Rama Rao, Deepak K. Pattanayak & Vanitha C, *Trans. of the Indian Inst. of Met.* **76** (2022) 271–277. https://doi.org/10.1007/s12666-022-02663-w.

17. Shakil S.I, Hadadzadeh A, Pirgazi H & Mohammadi M, Haghshenas M, *Micron,* **150** (2021) 103145,1-12. https://doi.org/10.1016/j.micron.2021.103145.

18. Sastry D H, *Mater. Sci. and Engg. A* **409**, (2005) 67-75. https://doi.org/10.1016/j.msea.2005.05.110

19. Zhuang F K, Tu S T, Zhou G Y &Wang Q Q, *The J. of Strain Analy. for Engg. Des.* **49**, (2014) 482-491. https://doi.org/10.1177/0309324714537056

20. Suryanarayana C, Grant Norton M, "X-Ray Diffraction: A Practical Approach", Springer New York, 1998, 207-221, ISBN: 97801489901484 https://doi.org/10.1007/978-1-4899-0148-4.

21. Bera S, Chowdhury S G, Estrin Y & Manna I, *J. Alloys Compd.* **548** (2013) 257-265. https://doi.org/10.3390/ma14020430.

22. Cahoon J R, Broughton W H & Kutzak A R, *Metall. Trans.* **2**, (1971) 1979. https://doi.org/10.1007/BF02913433

23. Fiocchi J, Tuissi A, Bassani P & Biffi C A, *J. Alloys Compd.* **695** (2017) 3402-3409. https://doi.org/10.1016/j.jallcom.2016.12.01.

24. Xianglong Yu & Wang Lianfeng, *Proced. Manuf.* **15** (2018) 1701-1707. https://doi.org/10.1016/j.promfg.2018.07.265.

25. Nesma T. Aboulkhair, IanMaskery, ChrisTuck, IanAshcroft & Nicola M.Everitt, *Mater. Sci. & Engg. A* **667** (2016) 139-146. https://doi.org/10.1016/j.msea.2016.04.092.

26. Li W, Li S, Liu J, Zhang A, Zhou Y, Wei Q, Yan C & Shi Y, *Mater. Sci. Eng. A* **663** (2016) 116-125. https://doi.org/10.1007/s42452-019-0270-5

27. Alghamdi F & Haghshena M, *SN Appl. Sci.* **1** (2019) 255-265. https://doi.org/10.1007/s42452-019-0270-5

28. Chen M & Goodman D W, *Chem. Soc. Rev.* **37** (9), (2008) 1860-1870. https://doi.org/10.1016/j.jcat.2013.11.020.

29. Iturrioz A, Gil E, Petite M M, Garciandia F, Mancisidor A M & San Sebastian M, *Weld. World* **62** (4), (2018) 885-892. https://doi.org/10.1007/s40194-018-0592-8

30. Michael Schuch, Tom Hahn & Matthias Beckman, *Mater. Sci. & Engg. A*, **813** (2021) 141134,273-286. https://doi.org/10.1016/j.msea.2021.141134.

31. Alghamdi F, Song X, Hadadzadeh A, Shalchi-Amirkhiz B, Mohammadi M & Haghshenas M, *Mate. Sci. & Engg. A*, **783** (2020) 139296,1-12. https://doi.org/10.1016/j.msea.2020.139296.

32. Takata N, Kodaira H, Sekizawa K, Suzuki A & Kobashi M, *Mater. Sci. and Engg.A* **704** (2017) 218–228. https://doi.org/10.1016/j.msea.2017.08.029

33. Aboulkhair N T, Tuck C, Ashcroft I, Maskery I & Everitt N M, *Metall. and Mater. Trans. A* **46** (2015) 3337–3341. https://doi.org/10.1007/s11661-015-2980-7.